

Article

# Structural, Optical, Band Edge and Enhanced Photoelectrochemical Water Splitting Properties of Tin-Doped WO<sub>3</sub>

Shankara S. Kalanur

Department of Materials Science and Engineering, Ajou University, Suwon 443-739, Korea;  
shankarask@ajou.ac.kr

Received: 11 May 2019; Accepted: 16 May 2019; Published: 17 May 2019



**Abstract:** The substitutional doping of tungsten oxide (WO<sub>3</sub>) with metal ions demonstrates a promising approach to enhance its photoelectrochemical (PEC) water splitting efficiency. In this article, the substitutional doping of Sn ions into WO<sub>3</sub> lattice and its effect on optical, electrical, band edge, and PEC water splitting properties are explored. Sn-doped WO<sub>3</sub> thin films were synthesized using a facile hydrothermal method. The characterization data reveal that the doping of Sn alters the morphology, induces multiple crystal phases, effects the crystal orientation, reduces the band gap, and increases the carrier density of WO<sub>3</sub>. With the uniform distribution of Sn ions in WO<sub>3</sub> and the decreased charge transfer resistance at the electrode/electrolyte interface, the doped WO<sub>3</sub> show notable enhancement in its PEC activity compared to the undoped WO<sub>3</sub>. The band edge study revealed that the introduction of Sn in WO<sub>3</sub> lattice causes an increase in the energy distance between the valence band edge and Fermi level and, at the same time, induces a downward shift in both the valence and conduction band edges towards higher potentials with respect to reversible hydrogen electrode (RHE). Conclusively, this work shows significant and new insights about Sn-doped WO<sub>3</sub> photoanodes and their influence on PEC water splitting efficiency.

**Keywords:** tungsten oxide; tin ions; photoelectrochemical water splitting; optical properties; band edge positions

## 1. Introduction

A promising resolution to the global energy requirement of the future, along with the protection of environment, comes from the next generation and sustainable energy source hydrogen and its clean and carbon-free production via photoelectrochemical water splitting [1]. In photoelectrochemical (PEC) water splitting, a semiconductor is used to split water into H<sub>2</sub> and O<sub>2</sub> using abundant and sustainable resources, like sunlight and water [2,3]. The first successful demonstration of solar water splitting using TiO<sub>2</sub> semiconductor was reported by Fujishima and Honda [4], and has initiated significant research attention and contributions that have continued until now. As a result, a variety of semiconductors were explored, researched, and reported as an active material for solar water splitting reaction. Notably, the well-matched optical, electrical properties, and stability of the metal oxides have demonstrated their active participation as useful electrode materials in PEC water splitting systems.

Among the various metal oxide materials utilized in PEC water splitting, tungsten oxide (WO<sub>3</sub>) has emerged as a promising candidate, due to its suitable physical and chemical properties [5,6]. The effective utilization of WO<sub>3</sub> in solar water splitting was first demonstrated in 1976 by Hodes et al. [7]. Since then, significant research contributions have been reported. It was found that WO<sub>3</sub> can absorb a maximum of ~12% of the incident solar light with a band gap of 2.6–2.8 eV. Ideally, based on its light absorption capability, as high as ~4.8% of solar energy to the hydrogen conversion efficiency could be

extracted [8]. However,  $\text{WO}_3$  faces numerous limitations that affect its charge generation, separation, and transportation properties, that decrease its ability to carry out water splitting. Therefore, the structural, optical, and electrochemical properties of  $\text{WO}_3$  need to be tuned to increase its water splitting efficiency.

The tuning of the structural, optical, and electrochemical properties of  $\text{WO}_3$  could be achieved by various modifications that improve its PEC water splitting efficiency. In particular, the crystal structure, band gap, carrier density, and charge transport at the electrolyte interface are the most significant factors influencing water splitting efficiency. Among the existing crystal structures, monoclinic  $\text{WO}_3$  is known to be the most suitable crystal phase for PEC water splitting [9–11]. Therefore, it is essential to explore the possible modification through which the structural, optical, and electrical properties of monoclinic  $\text{WO}_3$  could be tuned and optimized without disrupting the crystal nature and stability. Hence, an effectively tuned monoclinic  $\text{WO}_3$  is expected to be beneficial for the water splitting reaction, compared to undoped  $\text{WO}_3$ .

A recent study indicates that the substitutional doping of metal ions is an effective strategy of tuning the physical and chemical properties of  $\text{WO}_3$  [12–15]. Importantly, the type and extent of modification induced in doped  $\text{WO}_3$  mainly depend on the nature of dopant metal ion and its concentration [13,16,17]. Therefore, exploring a suitable dopant material for  $\text{WO}_3$  is essential for obtaining high efficiency in PEC water splitting [3]. Until now, various dopants, including Ti [16], Co [18], Mo [17], Zn [19], Bi [13], Ni [18], Nb [20], Cu [18], Al [21], Ta [22], Fe [23–25], Te [26], and Ba [27], have been employed to alter the structural, optical, electrical, and band edge properties of  $\text{WO}_3$  and to enhance its photocatalytic properties. Previously, Sn has been actively used as an effective dopant material for metal oxides, such as  $\text{Fe}_2\text{O}_3$ , to enhance its PEC water splitting properties [28,29], revealing its positive impact as a dopant material. Moreover, a detailed literature survey revealed that despite a few reports, no in-depth study has been reported regarding the synthesis and PEC properties Sn-doped  $\text{WO}_3$  thin films. Hence, it is essential to explore the effect of Sn doping on the structural, optical, electrical, band edge, and PEC water splitting properties of  $\text{WO}_3$ .

Given this, we here synthesize and explore the effect of Sn doping on the PEC water splitting efficiency of  $\text{WO}_3$  thin films. To obtain the Sn-doped  $\text{WO}_3$  thin films, a facile single-step hydrothermal approach is utilized, that is proceeded by introducing the Sn precursor into a peroxopolytungstic acid (PTA) solution, followed by reaction at 150 °C. The Sn-doped  $\text{WO}_3$  thin films were characterized in detail to understand the effect on structural, crystallographic, optical, and electrical properties of  $\text{WO}_3$ . Furthermore, Sn ions were found to be uniformly distributed in the  $\text{WO}_3$  crystals on the (fluorine doped tin oxide) FTO substrate, without affecting their adhesion. Using data from the absorbance, X-ray photoelectron spectroscopy, and Mott–Schottky (MS) analysis, an appropriate band edge positions of  $\text{WO}_3$  was plotted with respect to RHE potentials before and after doping with Sn ions. The electrochemical measurements revealed that Sn-doped  $\text{WO}_3$  thin films show increased photocurrent (at 1.23 V vs. RHE), incident photon-to-current efficiency (IPCE) and decreased charge transfer resistance across the electrode/electrolyte interface. The notable enhancement in the PEC properties of  $\text{WO}_3$  upon Sn doping was ascribed to the proper crystal facet orientation, decreased band gap, and significant increase of carrier density.

## 2. Results and Discussion

The hydrothermal synthesis method utilized in the present study allows for the precise tuning of Sn atom % in the  $\text{WO}_3$  lattice by controlling the Sn precursor concentration in the hydrothermal synthesis solution. Table S1 shows the amount of precursor solution taken in the synthesis solution and the atom % and wt % of Sn detected via EDS. Based on the PEC studies, the  $\text{WO}_3$  thin films doped with 0.8 atom % of Sn showed enhanced photocurrent compared to the samples doped with the other concentrations of Sn, and hence, were chosen for detailed characterization. Figure 1 shows the high- and low-resolution SEM images of undoped and Sn-doped  $\text{WO}_3$  thin films. The morphology of undoped  $\text{WO}_3$  (Figure 1a,b) appeared to be a mixture of nanoparticles, and nanorod structure assembled on the FTO substrate.

After Sn doping, a significant change in morphology was observed, indicating the disappearance of nanorod morphology and the formation of smaller (5–10 nm) coagulated nanoparticles (Figure 1d,e) and the presence of larger (500–1000 nm) nanoparticles and plates at different places. This suggests that the substitution of Sn in crystal lattice affects the structure of  $\text{WO}_3$ . The cross-section SEM image of undoped  $\text{WO}_3$  (Figure 1c) clearly shows the nanorod morphology assembled on the thin film of the nanoparticle layer. The thickness of the thin film was measured to be  $\sim 2 \mu\text{m}$ . Figure 1f shows the cross-section SEM image of Sn-doped  $\text{WO}_3$  thin film, confirming the change in morphology and the decrease in film thickness to  $1 \mu\text{m}$ . Furthermore, the low-resolution SEM image confirmed the uniform deposition of doped  $\text{WO}_3$  throughout the FTO substrate with a reduced thickness, indicating that the doping of Sn affects the deposition amount of  $\text{WO}_3$  on the substrate.

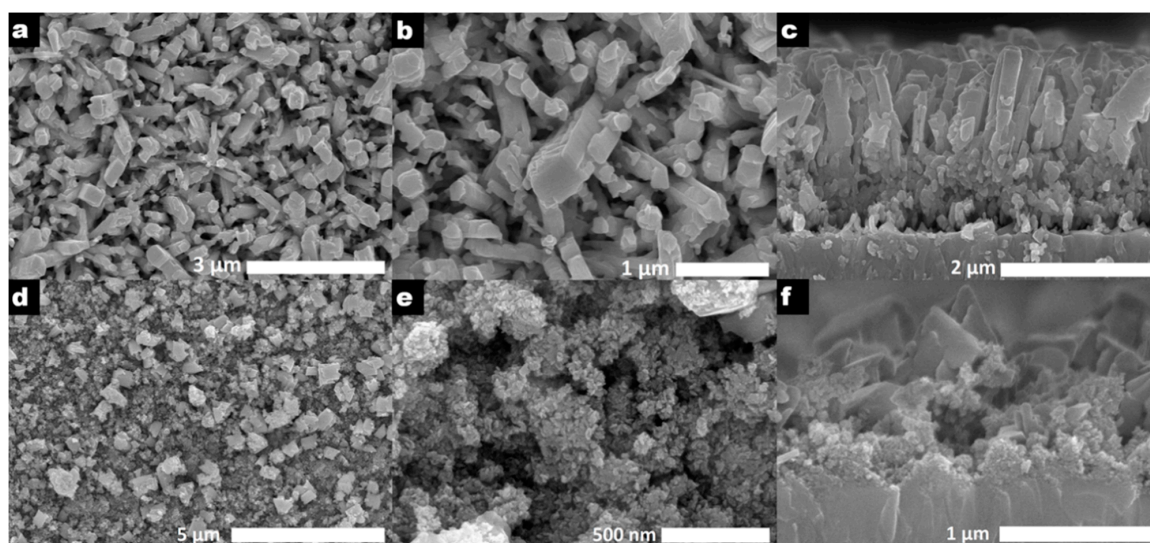


**Figure 1.** Low (a,d) and high (b,e) resolution surface and (c,f) cross-section SEM images of undoped and Sn-doped  $\text{WO}_3$ , respectively.

It is well known that the  $\text{WO}_3$  thin films synthesized by hydrothermal treatment of PTA solution produce orthorhombic  $\text{WO}_3 \cdot 0.33\text{H}_2\text{O}$  that is converted to anhydrous monoclinic  $\text{WO}_3$  upon annealing at  $500^\circ\text{C}$ . Figure 2a confirms that the synthesized undoped  $\text{WO}_3$  thin films (annealed at  $500^\circ\text{C}$ ) showed monoclinic crystal structure (with lattice parameters of  $a = 0.729 \text{ nm}$ ,  $b = 0.753 \text{ nm}$ ,  $c = 0.767 \text{ nm}$ , and  $\beta = 90.92^\circ$ ) by producing three characteristics peaks related to [002], [020], and [200] plane at  $2\theta$  degree value of 23.18, 23.63, and 24.41 (JCPDS no. 43–1035), respectively. In Figure 2, the peaks arising from the FTO substrate ( $\text{SnO}_2$ ) are indicated with black dots, whereas the monoclinic peaks of  $\text{WO}_3$  are marked with green star marks. Moreover, due to the dominant appearance of substrate  $\text{SnO}_2$  peaks, the diffraction lines related to the very low concentration of doped  $\text{SnO}_2$  peaks were expected to merge and are indistinguishable. Notably, the XRD peaks of the FTO substrate appeared comparatively intense in doped  $\text{WO}_3$  compared to undoped  $\text{WO}_3$ , due to the reduced thickness of  $\text{WO}_3$  film in the Sn-doped samples, as observed in Figure 1f. Careful observation of the XRD data of Sn-doped  $\text{WO}_3$  thin films (Figure 2b) revealed few critical changes in the diffraction patterns. Firstly, the peak positions of [002], [020], and [200] planes of monoclinic  $\text{WO}_3$  (with lattice parameters of  $a = 0.729 \text{ nm}$ ,  $b = 0.753 \text{ nm}$ ,  $c = 0.767 \text{ nm}$ , and  $\beta = 90.92^\circ$ ) show a significant shift towards higher  $2\theta$  degree values. That is, the peak positions of [002], [020], and [200] planes were found to be shifted to 23.39, 23.80, and 24.56 of  $2\theta$  degree values, respectively, after Sn doping (Figure S1). This indicates that the doping of Sn takes places by displacing a few of the W ions from their lattice positions.

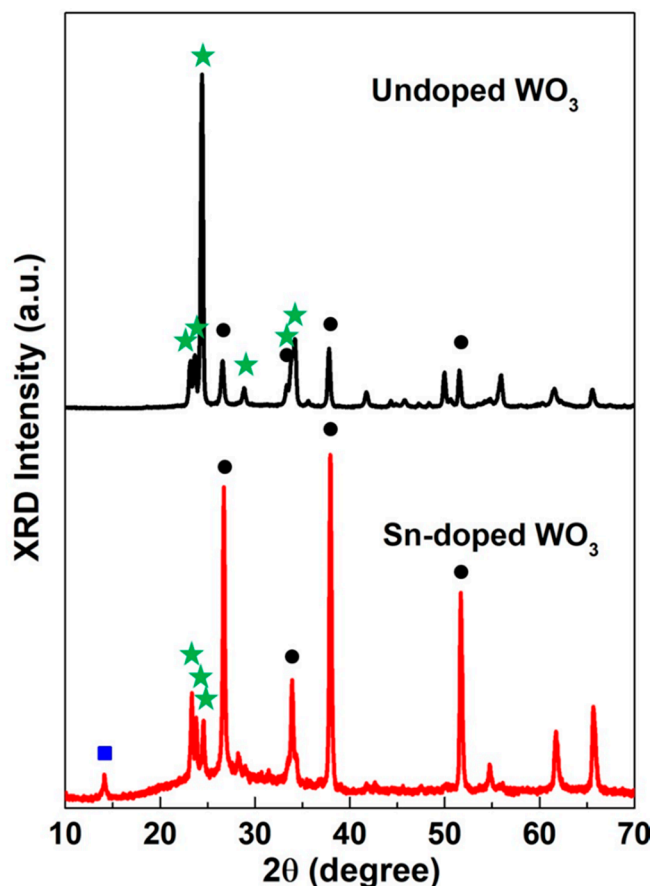


**Figure 2.** XRD patterns of undoped and Sn-doped  $\text{WO}_3$  thin films. The XRD peaks of FTO substrate and monoclinic and hexagonal  $\text{WO}_3$  are indicated by a dot (black), star (green) and square (blue) marks.

The most significant change observed in the XRD pattern of  $\text{WO}_3$  after Sn doping was in the peak intensities related to [002], [020], and [200] planes. The peak height associated with the different planes in the XRD pattern suggests the crystal growth direction. Interestingly, the PEC water splitting efficiency of  $\text{WO}_3$  depends on the crystal plane orientation [30]. As reported previously, a [002] plane-oriented  $\text{WO}_3$  crystal is beneficial, and performs an efficient water oxidation reaction at the surface and eventually shows higher PEC water splitting efficiency compared to the [020] and [200] plane-oriented crystals. The XRD pattern of undoped  $\text{WO}_3$  reveals the dominant and most intense peak of the [200] plane, which is reported to be a non-suitable orientation for the PEC water splitting reaction. However, upon Sn doping, a significant decrease in [200] peak and an increase in [002] was observed. This indicates that doping of Sn promotes the preferred growth direction of  $\text{WO}_3$  crystals towards the [002] orientation, from the [200] plane, and could influence its PEC water splitting efficiency. In addition to the above changes, the doping of Sn tends to induce multiple phases in  $\text{WO}_3$  as noted from the appearance of new XRD peak at a low diffraction angle, which is ascribed to the hexagonal phase of  $\text{WO}_3$ . The presence of a peak related to the hexagonal phase of  $\text{WO}_3$  was due to the reconstructive transformation process that occurs during the annealing step.

As described in earlier reports, the hydrothermal treatment of PTA solution produces  $\text{WO}_3 \cdot 0.33\text{H}_2\text{O}$  (orthorhombic phase), that undergoes a reconstructive transformation during the calcination step [31]. In particular, the reconstructive transformation involves temperature dependence, breaking of bonds, elimination of a water molecules, and a change in crystal structure with the formation of new bonds [31]. Briefly, annealing of  $\text{WO}_3 \cdot 0.33\text{H}_2\text{O}$  at  $500\text{ }^\circ\text{C}$  transforms the orthorhombic phase to hexagonal phase (at  $400\text{ }^\circ\text{C}$ ), and then to stable monoclinic phase (at  $500\text{ }^\circ\text{C}$ ). However, the doping of Sn ions in  $\text{WO}_3 \cdot 0.33\text{H}_2\text{O}$  (orthorhombic structure) will result in obstruction of the reconstructive transformation during calcination. Hence, the partial transformation from hexagonal to monoclinic phase takes place,

resulting in multiple structures in the product. In fact, the interference of doped metal ions during reconstructive transformation, causing multiple phases of  $\text{WO}_3$ , has already been observed before [16].

The low-resolution TEM images shown in Figure 3a,c indicate the nanorod and particle morphology of undoped and Sn-doped  $\text{WO}_3$  thin films, respectively. In the high-resolution TEM image of undoped  $\text{WO}_3$ , a  $d$ -spacing value of 0.3645 was calculated (Figure 3b) which was ascribed to the [200] plane of monoclinic  $\text{WO}_3$ . The  $d$ -spacing value of Sn-doped  $\text{WO}_3$  was estimated to be 0.3634 nm (Figure 3d), which was noted to be slightly less than undoped  $\text{WO}_3$ . The slight decrease in  $d$ -spacing value agrees with the shift in diffraction angles to the higher degree observed in the XRD patterns after Sn doping, and hence confirms the insertion of Sn ions into the  $\text{WO}_3$  lattice. The distribution of Sn ions in  $\text{WO}_3$  lattice was observed by collecting elemental mapping data attached to the TEM. In the selected area (Figure 4a) of the Sn-doped  $\text{WO}_3$  samples, the elemental mapping showed a uniform distribution of W (Figure 4b), O (Figure 4c), and Sn (Figure 4d), and the EDS measurement (Figure 4e) confirmed atom % and wt % of individual elements and the absence of impurities. The UV-vis absorption spectra of undoped  $\text{WO}_3$  shows the absorption onset of 470 nm, as shown in Figure 5a. Upon Sn doping, a very slight redshift in absorption onset to 500 nm was observed (Figure 5a). In addition, the doping of Sn tends to cause tailing of absorbance onset into the visible region, indicating an increase in oxygen vacancies. The Tauc plot shown in Figure 5b confirms the reduction in band gap from 2.62 to 2.46 eV for undoped  $\text{WO}_3$  and Sn-doped  $\text{WO}_3$  thin films, respectively.

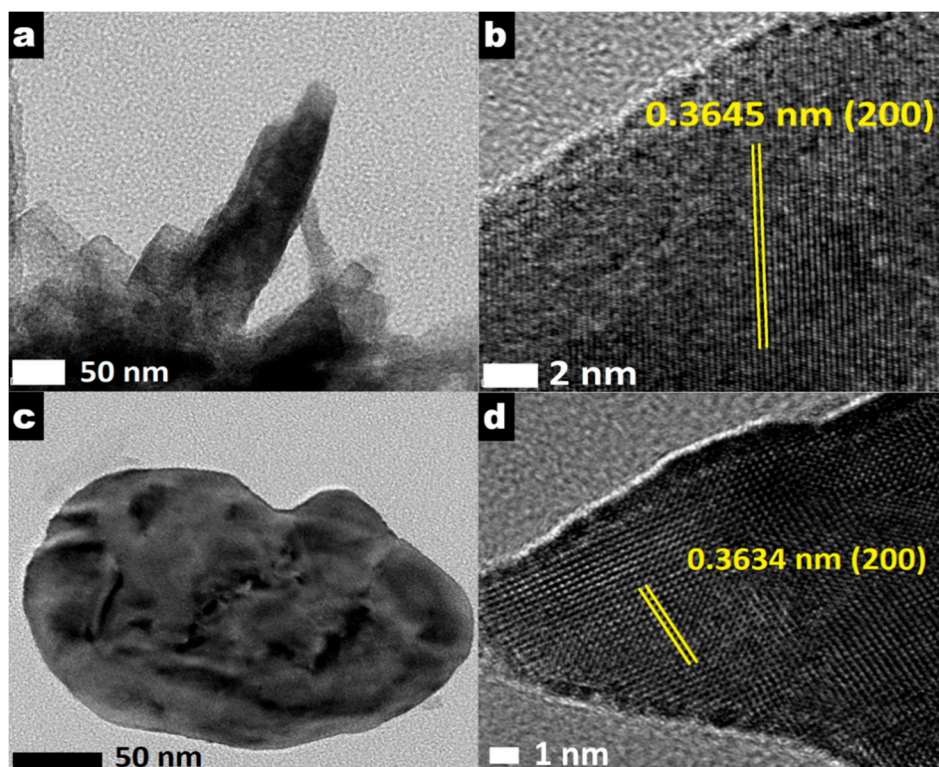


**Figure 3.** Low (a) and high (b) resolution TEM images of undoped  $\text{WO}_3$  showing the  $d$ -spacing value of 0.3645 nm ascribed to [200] plane of monoclinic  $\text{WO}_3$ . (c) Low- and (d) high-resolution TEM image of Sn-doped  $\text{WO}_3$  exhibiting the  $d$ -spacing value of 0.3634 nm.

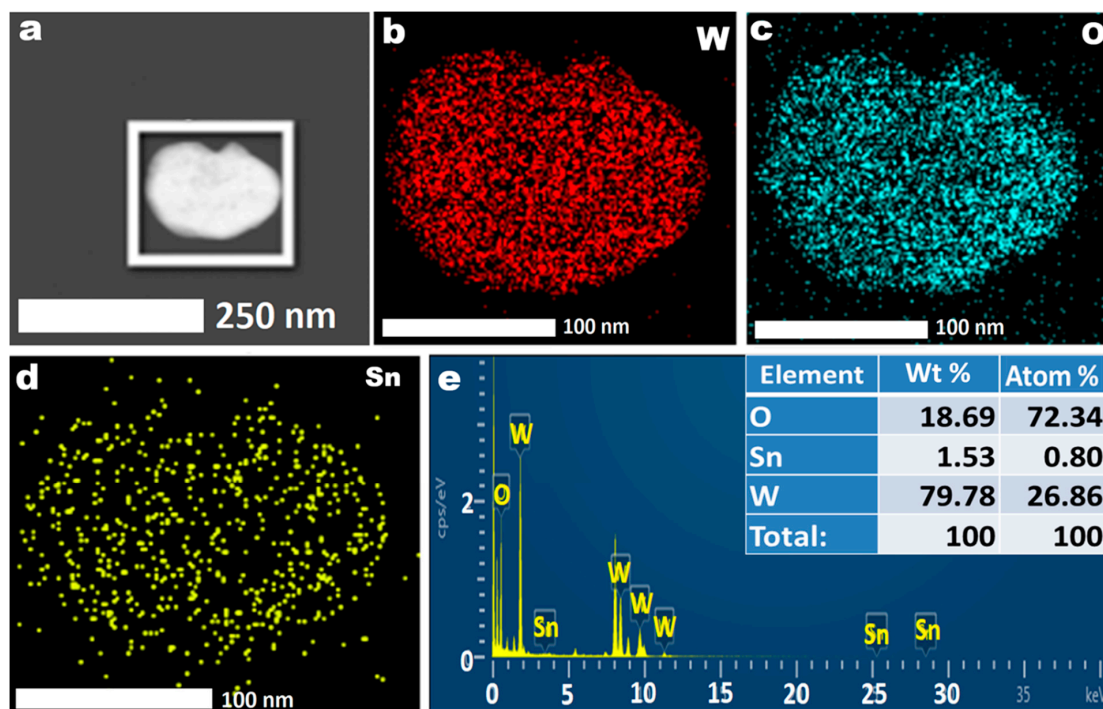


**Figure 4.** (a) Scanning transmission electron microscopy (STEM) image showing the selected area of Sn-doped  $\text{WO}_3$  nanoparticle and elemental mapping indicating the distribution of (b) W, (c) O, and (d) Sn. (e) EDS graph and the inset table show the quantitative values of elements present in the Sn-doped  $\text{WO}_3$  nanoparticle.

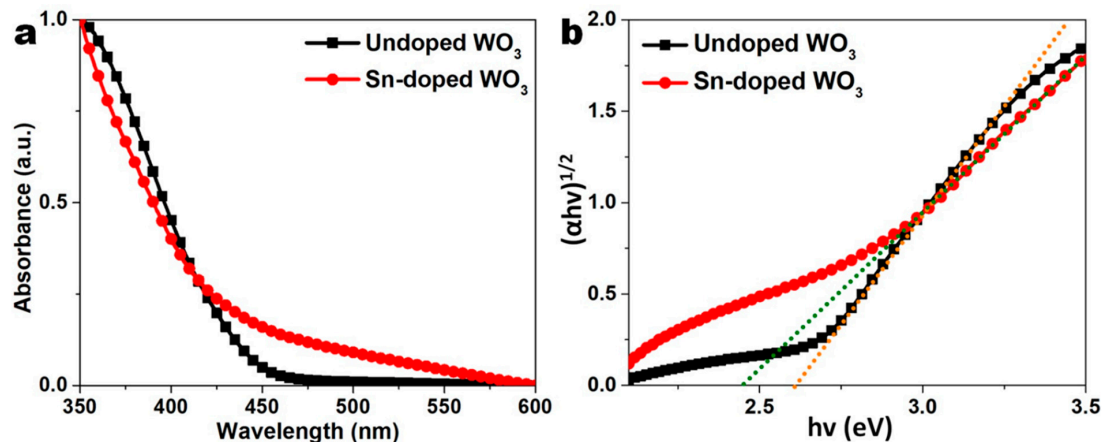


**Figure 5.** (a) UV-vis absorption spectra and (b) Tauc plot of undoped (black) and Sn-doped  $\text{WO}_3$  (red) thin films.

The XPS survey spectrum of Sn-doped  $\text{WO}_3$  thin films is shown in Figure 6a, indicating the presence of W, O, and Sn without any impurities. The doping of metal ions is reported to alter the concentration of oxygen vacancies in  $\text{WO}_3$ . Hence, the high-resolution W 4f core-level XPS spectra were deconvoluted as shown in Figure 6b,c. In the high-resolution XPS W 4f core-level spectra, two major peaks were detected, and were assigned to  $\text{W}^{6+}$  state (at 35.25 and 37.40 eV of binding energy) of  $4f_{7/2}$  and  $4f_{5/2}$ . In addition to the two major peaks mentioned above, two low-intensity peaks were obtained that are ascribed to the presence of  $\text{W}^{5+}$  state (at binding energy values of 33.95 and 36.10 eV), and hence, the presence of oxygen vacancies (i.e., causing a partial reduction of  $\text{W}^{6+}$ ) were confirmed. Similarly, the deconvolution of W 4f core-level XPS spectra of Sn-doped  $\text{WO}_3$  revealed two doublets each for  $\text{W}^{6+}$  and  $\text{W}^{5+}$  state. However, careful observation revealed that the peak intensity of  $\text{W}^{5+}$  state

shows a significant increase after Sn doping. Precisely, the peak area of  $W^{5+}$  state in undoped  $WO_3$  was calculated to be 0.82% and 1.12%, corresponding to  $W 4f_{5/2}$  and  $W 4f_{7/2}$  states, respectively, and was found to be increased to 6.22% and 4.68% with respect to  $W 4f_{5/2}$  and  $W 4f_{7/2}$  state, respectively, for the Sn-doped  $WO_3$ . This indicates a drastic increase in the oxygen vacancies in  $WO_3$  after Sn doping. This could be due to the change in the valence state of dopant Sn ion and the host W ions. Furthermore, in the high-resolution XPS spectra of  $W 4f$ , a significant shift in the peak positions of  $W^{6+}$  and  $W^{5+}$  states towards higher binding energy was observed. This indicates that the doping of Sn takes place by replacing W atoms via substitutional doping [32]. The high-resolution XPS spectra of Sn shows (Figure 6d) two peaks at binding energy values of 485.5 and 494.5 eV, with spin-orbit components of 8.4 eV, corresponding to  $3d_{3/2}$  and  $3d_{5/2}$  core levels. Furthermore, the peak fitting deconvolution produced two doublets corresponding to the Sn(II) and Sn(IV) states. However, the presence of Sn(II) was observed to be dominant compared to the Sn(IV) state [33].

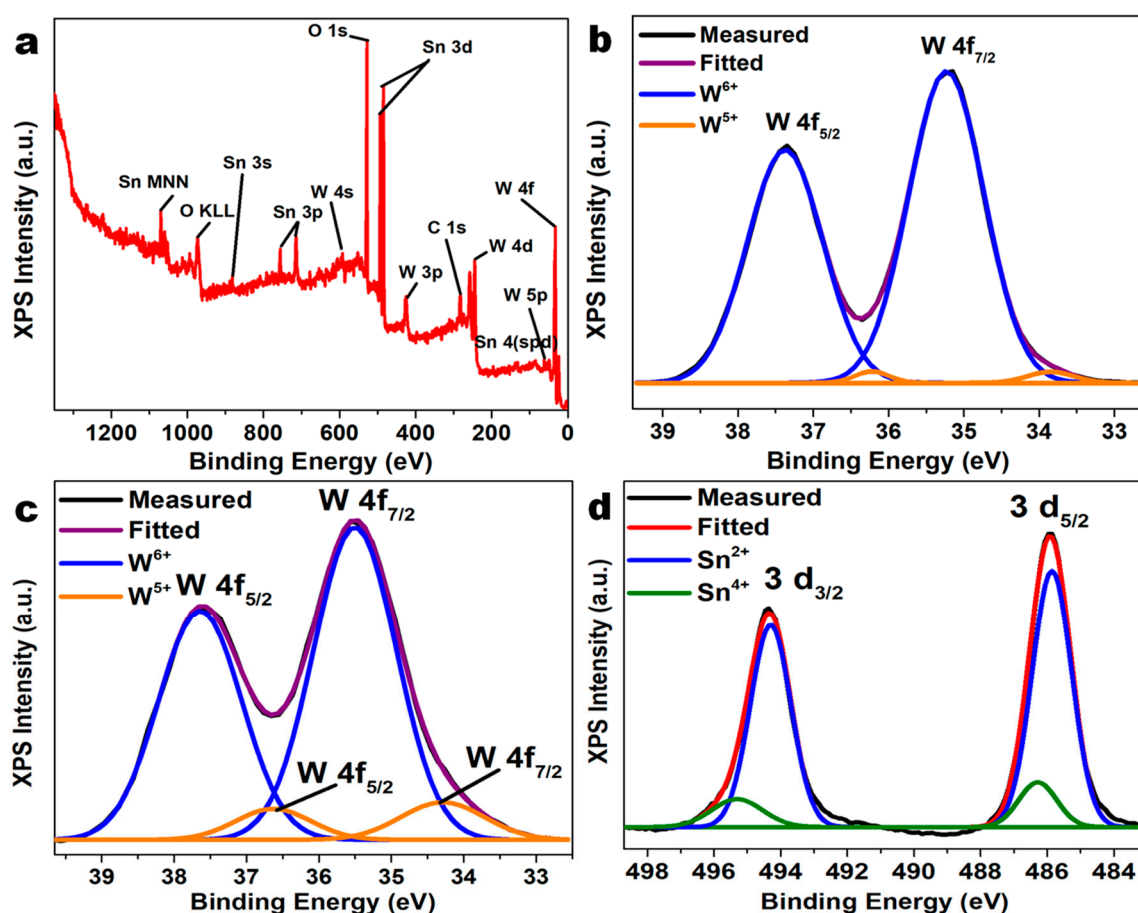


**Figure 6.** (a) XPS survey spectrum of the Sn-doped  $WO_3$  thin film. Deconvoluted high-resolution XPS spectra of  $W 4f$  core level of (b) undoped and (c) Sn-doped  $WO_3$ . (d) Deconvoluted high-resolution XPS spectra of Sn  $3d$  core levels.

The Fermi-level position of  $WO_3$  is sensitive to its crystal environment and constituent atoms. Hence, doping  $WO_3$  tends to alter its Fermi energy level with respect to valence and conduction band edge positions. Using XPS valence band edge analysis, the energy difference between the Fermi level and the valence band edge was determined for both the undoped and Sn-doped  $WO_3$ . Figure 7a,b shows the XPS valence band edge plot. The undoped  $WO_3$  show 2.07 eV energy difference between the valence band and Fermi level that increased to 2.21 eV upon Sn doping. The significant increase in energy difference tends to push the Fermi level towards and near the conduction band edge position. Hence, Sn-doped  $WO_3$  is expected to behave more n-type compared to undoped  $WO_3$ .

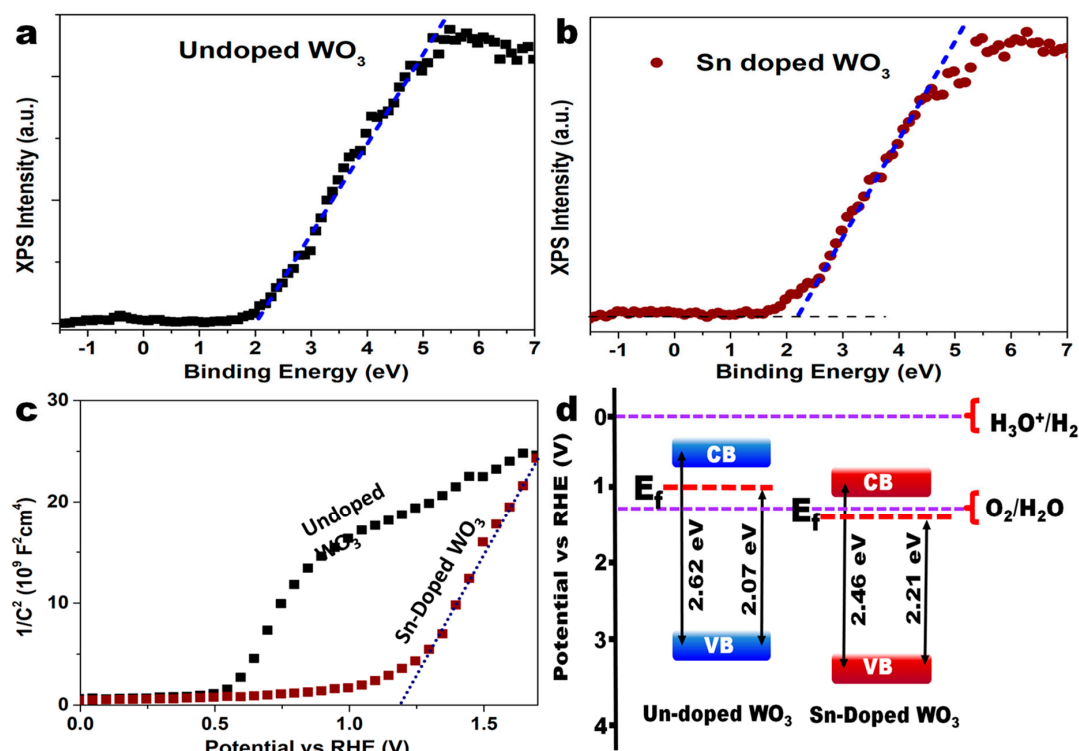


**Figure 7.** XPS valence band edge plot of (a) undoped and (b) Sn-doped WO<sub>3</sub> thin films. (c) Mott–Schottky plot of undoped and Sn-doped WO<sub>3</sub> thin films. (d) Band edge position of WO<sub>3</sub> plotted against RHE before and after doping with Sn.

The Mott–Schottky (MS) plot was used to understand the band edge positions of WO<sub>3</sub> with respect to RHE values and water splitting potentials. Also, the carrier density could be determined using MS plots. The MS experiments were carried out in the dark in 0.5 M Na<sub>2</sub>SO<sub>4</sub> at 1000 Hz of frequency using the equation

$$1/C^2 = [2/(N_D e \epsilon_0 \epsilon)] [(V_S - V_{FB}) - (k_B T/e)], \quad (1)$$

where  $C$ ,  $N_D$ ,  $e$ ,  $\epsilon_0$ ,  $\epsilon$ ,  $V_S$ ,  $V_{FB}$ ,  $k_B$ , and  $T$  are the space charge capacitance, carrier density, elementary charge, permittivity of the vacuum, the relative permittivity of WO<sub>3</sub>, applied potential, flat band potential, Boltzmann constant, and temperature (299 K), respectively. Using the slope and intercept of the plot of  $1/C^2$  vs. applied potential (Figure 7c),  $N_D$  and  $V_{FB}$  were calculated. The  $V_{FB}$  and  $N_D$  values of undoped and Sn-doped WO<sub>3</sub> were obtained as 0.54 V (vs. RHE),  $6.35 \times 10^{17} \text{ cm}^{-3}$  and 1.21 V (vs. RHE),  $8.38 \times 10^{17} \text{ cm}^{-3}$ , respectively.

The flat band potential values obtained using MS plots suggest the position of conduction band edge position of WO<sub>3</sub>. Precisely, for the n-type semiconductors, the conduction band edge could be positioned at slightly lower potential with respect to its flat band potential [34]. Therefore, the conduction band edge of WO<sub>3</sub> is expected to be placed at less than 0.1 V of its flat band potentials [35]. Based on the flat band edge potentials, the conduction band edge of undoped and Sn-doped WO<sub>3</sub> was determined to be at 0.44 and 1.11 V vs. RHE, respectively. Subsequently, the positions of valence band edge position with respect to RHE were calculated using the band gap values (Figure 5) and conduction band edge positions. Figure 7d shows the band edge diagram of undoped and Sn-doped WO<sub>3</sub> plotted against RHE values and with reference to the overall water splitting potentials. Note that the positions of Fermi levels were also included, based on the XPS results. Overall, the band edge plot indicates that the doping of Sn pushes both the conduction and valence band edge of WO<sub>3</sub> towards higher potentials. At the same time, the Fermi level shifts upward towards the conduction band edge position, making it more n-type compared to the undoped WO<sub>3</sub>. Such an observation was

evident as the doping of post-transition metal ions into  $\text{WO}_3$  shift its band edge positions towards higher potentials as previously observed in case of Bi dopant [13]. In general, it can be concluded that the doping of post-transition metal atoms into  $\text{WO}_3$  causes a downward shift in band edge positions towards higher potentials and increases the carrier density in  $\text{WO}_3$ .

The enhancement in PEC properties of Sn-doped  $\text{WO}_3$  was evaluated by measuring linear sweep voltammetry (LSV) of doped  $\text{WO}_3$  photoanode by exposing the 1.5 G illumination in 0.5 M  $\text{Na}_2\text{SO}_4$  electrolyte. Figure 8a depicts the LSV plots of undoped and Sn-doped  $\text{WO}_3$  thin films. The substitutional doping of Sn in  $\text{WO}_3$  was found to increase the photocurrent to  $0.427 \text{ mA cm}^{-2}$  from  $0.253 \text{ mA cm}^{-2}$  (at 1.23 V vs. RHE) of undoped  $\text{WO}_3$ . As shown in Figure S2, the photocurrent of  $\text{WO}_3$  increases with the increase in atom % of doped Sn. The highest photocurrent was recorded at 0.80 atom % of Sn-doped  $\text{WO}_3$ . The IPCE measurements were recorded to understand the PEC behavior with respect to incident light wavelength using the below equation.

$$\text{IPCE} = (1240I)/(\lambda P), \quad (2)$$

where  $I$ ,  $\lambda$ , and  $P$  refers to the current density ( $\text{mA cm}^{-2}$ ) recorded at 1.23 V vs. RHE, the wavelength of incident light (nm), and power density at a given wavelength ( $\text{mW cm}^{-2}$ ), respectively. The IPCE plots shown in Figure 8b confirm that doping of Sn increases the IPCE values to 44% (at 300 nm) along with the slight redshift of onset absorbance. This suggests that Sn-doped  $\text{WO}_3$  yields significantly higher currents than the undoped  $\text{WO}_3$  at higher wavelengths. The calculated IPCE data were integrated between the wavelength range of 300 to 600 nm using standard values of AM 1.5 G data. The integrated plots, along with the IPCE data in Figure 8b, validate the photocurrent values obtained using the solar simulator. That is, the integrated photocurrents values were in a good agreement with the values recorded in the LSV plots. Figure 8c shows Nyquist plots of the undoped and Sn-doped  $\text{WO}_3$  samples. The plots indicate that the 0.80 atom % Sn-doped  $\text{WO}_3$  shows smaller semicircle and offers lower charge transfer resistance compared to the undoped  $\text{WO}_3$  at the interface of electrode and electrolyte.

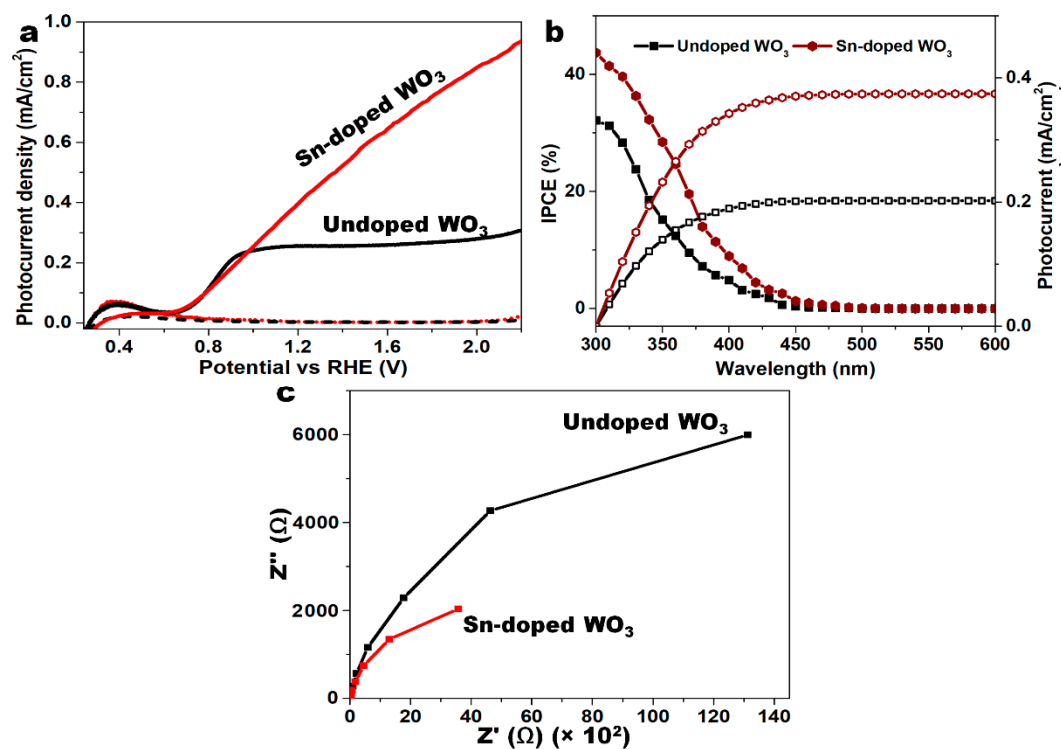


**Figure 8.** (a) Linear sweep voltammetry (LSV) plots (dotted lines indicated LSV measured in the dark), (b) incident photon-to-current efficiency (IPCE) and integrated IPCE, and (c) Nyquist plots of the undoped and Sn-doped  $\text{WO}_3$  thin films measured in 0.5 M  $\text{Na}_2\text{SO}_4$ .

Furthermore, the stability and gas evolution amount of undoped and Sn-doped WO<sub>3</sub> thin films were measured, and the results are shown in Figure 9. Both photoanodes exhibited good stability under continuous illumination of AM 1.5 G sunlight at a constant bias potential of 1.23 V vs. RHE (Figure 9a). This indicates that both the undoped and Sn-doped WO<sub>3</sub> thin films show significant stability during water splitting. Moreover, the evolution of O<sub>2</sub> gas during the water splitting were measured using GC. As shown in the Figure 9b, the Sn-doped WO<sub>3</sub> show significant increase in the O<sub>2</sub> evolution rate compared to the undoped WO<sub>3</sub>. Note that the valence band edge position of both undoped and Sn-doped WO<sub>3</sub> allow the spontaneous evolution O<sub>2</sub> gas only, and the H<sub>2</sub> gas was not detected due to its unsuitable conduction band edge position and low level of produced photocurrents. The faradaic efficiencies for the O<sub>2</sub> production was calculated using the following equation:

$$\text{Faradaic efficiency} = (4F \times n_{\text{O}_2})/Q, \quad (3)$$

where,  $F$ ,  $n_{\text{O}_2}$ , and  $Q$  are defined as the Faraday constant, amount of O<sub>2</sub> (mol), and amount of charge (C), respectively. The faradaic efficiencies of undoped and Sn-doped WO<sub>3</sub> were calculated to be 85% and 89%, respectively.

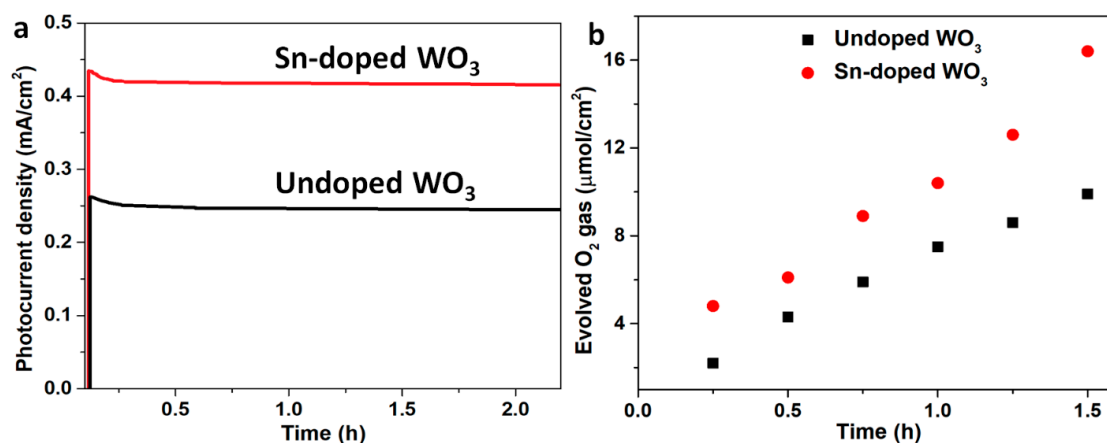


**Figure 9.** (a) Transient voltammogram of undoped and Sn-doped WO<sub>3</sub> thin films measured under AM 1.5 G illumination at an applied bias potential of 1.23 V RHE. (b) The evolution of O<sub>2</sub> gas at the photoanode measured for undoped and Sn-doped WO<sub>3</sub> under AM 1.5 G illumination at an applied bias potential of 1.23 V RHE using GC.

The enhancement in PEC properties of WO<sub>3</sub> after Sn doping was ascribed to several factors, based on the characterization results. Specifically, the orientation of crystal facet-induced band gap reduction, increase in carrier density, and the reduced charge transfer resistance were the main influencing factors for PEC activity. That is, the change in crystal facet orientation from [200] to [002] direction significantly increases water oxidation reaction kinetics at the electrode interface. This was notably evident from the impedance measurements exhibiting reduced charge transfer resistance across the interface. The optical data suggest that Sn-doped WO<sub>3</sub> is capable of absorbing significantly more incident light compared to the undoped electrode, which also affects its photocatalytic properties. Notably, the increase in oxygen vacancies in WO<sub>3</sub> after Sn doping extends the light-harvesting ability to the visible and near-infrared region [11]. Consequently, the increase in oxygen vacancies tends to elevate the donor density levels in WO<sub>3</sub> as evident from the MS studies, and also improves the conductivity and enhances the PEC water splitting activities [3].

### 3. Materials and Methods

The thin films of Sn-doped WO<sub>3</sub> on FTO were synthesized using an earlier reported hydrothermal method, with minor modifications [27]. The tin(II) chloride dihydrate (Sigma-Aldrich ≥99.0%, St. Louis, MI, USA) precursor was employed as the source of Sn dopant in WO<sub>3</sub>. The doping of Sn was achieved

during the hydrothermal reaction of PTA solution at 150 °C (for 3 h) in the presence of Sn ions of desired concentrations. The amount of Sn dopant in WO<sub>3</sub> was varied by controlling the concentration of tin(II) chloride dihydrate in PTA solution as described in Table S1. During the hydrothermal reaction, the FTO substrate was placed vertically in the Teflon container with its conducting side facing downwards. The synthesized undoped and doped thin films were annealed at 500 °C for 2 h. For the detailed characterization, the Sn-doped WO<sub>3</sub> (0.80 atom %) thin film that showed the highest PEC activity was chosen.

A MiniFlex desktop XRD instrument from Rigaku (Tokyo, Japan) was used to analyze the crystalline properties of synthesized thin films between the 10° and 90° diffraction angle (2θ). The morphology and distribution of dopants in WO<sub>3</sub> were investigated using a Hitachi S4800 (Tokyo, Japan) scanning electron microscope (SEM) and a JEOL JEM-2100F (Peabody, MA, USA) transmission electron microscope (TEM). The optical properties were explored using a Varian Cary 5000 spectrophotometer (Sydney, Australia). A Thermo Fisher Scientific (Waltham, MA, USA) instrument was utilized to analyze the valency and valence band edge properties. Linear sweep, transient and impedance measurements were carried out using an IviumStat (Eindhoven, Netherlands) electrochemical interface. The ABET Technologies Sun 2000 solar simulator (ABET Technologies, USA) calibrated to AM 1.5G was used as a light source. For IPCE measurements, a xenon arc lamp (1000 W) connected to a Thermo Oriel 66902 monochromator (Thermo Oriel Cornerstone 7400 1/8, USA) was used. The O<sub>2</sub> gas evolved during the water splitting reaction was measured by using a YOUNG LIN YL 6500 gas chromatograph (GC) (Anyang, South Korea). Helium gas was used as a carrier medium in the capillary column, and a pulsed discharge ionization detector (PDD) was used to detect evolved O<sub>2</sub> gas. For the PEC measurements, a three-electrode system setup was selected in a quartz cell with fabricated WO<sub>3</sub> thin film as photoanode, Pt counter electrode, and Ag/AgCl reference electrode. All electrochemical measurements were carried out in 0.5 M Na<sub>2</sub>SO<sub>4</sub> electrolyte. The reaction cell was thoroughly sealed, and the evolved O<sub>2</sub> gas was fed to GC using a pump with carrier gas. For the impedance measurements under illumination, a frequency range of 0.1–10<sup>5</sup> Hz with AC voltage perturbation of 10 mV was used. The MS analysis was carried out in the dark at a frequency of 1000 Hz. The Nernst equation was used to convert the measured potential to RHE values.

#### 4. Conclusions

Sn-doped WO<sub>3</sub> thin films were hydrothermally synthesized, and their PEC water splitting properties were explored. The uniform and substitutional doping of Sn in the WO<sub>3</sub> lattice was found to influence its morphology and crystal orientation. A slight reduction in the band gap was observed, along with the significant increase in the oxygen vacancies. The presence of Sn with a valency of (II) and (IV) in the WO<sub>3</sub> lattice was confirmed via XPS studies. The MS plots revealed an anodic shift in the flat band potential and increase in the carrier densities. The band edge diagram of WO<sub>3</sub> before and after Sn doping was plotted using XPS valence band edge, MS, and absorbance data. Based on this, a downward shift of both the valence and conduction band edge was revealed with a more n-type character of Sn-doped WO<sub>3</sub>. The PEC studies carried out in 0.5 M Na<sub>2</sub>SO<sub>4</sub> indicated that Sn-doped WO<sub>3</sub> performs significantly better as a photoanode than the undoped WO<sub>3</sub>. The synergic effect of Sn doping yields increased photocurrent and incident photon-to-current efficiency values. The results of this work conclude that Sn-doped WO<sub>3</sub> performs as superior photoanode and could be utilized in performing efficient PEC water splitting. Furthermore, the scheme proposed in this article will benefit future research in fabricating more efficient WO<sub>3</sub> photoanodes for PEC water splitting reactions.

**Supplementary Materials:** The following are available online at <http://www.mdpi.com/2073-4344/9/5/456/s1>, Table S1: The concentrations of tin (II) chloride dihydrate precursor added to PTA solution to obtain doped WO<sub>3</sub> having the below atom % and wt % of Sn. Figure S1: XRD pattern of undoped and Sn-doped WO<sub>3</sub> thin films magnified in the 2θ degree values of 21 to 26 indicating the shift in diffraction lines. Figure S2: Plot of photocurrent measured at 1.23 V vs RHE for the WO<sub>3</sub> samples doped with various atom % of Sn.

**Acknowledgments:** This work was supported by the Basic Research & Development program [NRF-2017R1D1A1B03035201] of the Ministry of Science and ICT, Republic of Korea. This work was also supported by Ajou University.

**Conflicts of Interest:** The authors declare no conflict of interest.

## References

1. Datt Bhatt, M.; Sung Lee, J. Recent theoretical progress in the development of photoanode materials for solar water splitting photoelectrochemical cells. *J. Mater. Chem. A* **2015**, *3*, 10632–10659. [[CrossRef](#)]
2. Walter, M.G.; Warren, E.L.; McKone, J.R.; Boettcher, S.W.; Mi, Q.; Santori, E.A.; Lewis, N.S. Solar water splitting cells. *Chem. Rev.* **2010**, *110*, 6446–6473. [[CrossRef](#)] [[PubMed](#)]
3. Kalanur, S.S.; Duy, L.T.; Seo, H. Recent progress in photoelectrochemical water splitting activity of WO<sub>3</sub> photoanodes. *Top. Catal.* **2018**, *1*–34. [[CrossRef](#)]
4. Fujishima, A.; Honda, K. Electrochemical photolysis of water at a semiconductor electrode. *Nature* **1972**, *238*, 238037a0. [[CrossRef](#)]
5. Di Valentin, C.; Pacchioni, G. Spectroscopic properties of doped and defective semiconducting oxides from hybrid density functional calculations. *Acc. Chem. Res.* **2014**, *47*, 3233–3241. [[CrossRef](#)] [[PubMed](#)]
6. Kalanur, S.S.; Seo, H.; Kalanur, S.S. Recent developments in photoelectrochemical water-splitting using WO<sub>3</sub>/BiVO<sub>4</sub> heterojunction photoanode: A review. *Mater. Sci. Energy Technol.* **2018**, *1*, 49–62.
7. Cahen, D.; Hodes, G.; Manassen, J. Tungsten trioxide as a photoanode for a photoelectrochemical cell (PEC). *Nature* **1976**, *260*, 312.
8. Liu, X.; Wang, F.; Wang, Q. Nanostructure-based WO<sub>3</sub> photoanodes for photoelectrochemical water splitting. *Phys. Chem. Chem. Phys.* **2012**, *14*, 7894–7911. [[CrossRef](#)] [[PubMed](#)]
9. Song, J.; Huang, Z.-F.; Pan, L.; Zou, J.-J.; Zhang, X.; Wang, L. Oxygen-deficient tungsten oxide as versatile and efficient hydrogenation catalyst. *ACS Catal.* **2015**, *5*, 6594–6599. [[CrossRef](#)]
10. Huang, Z.-F.; Song, J.; Pan, L.; Zhang, X.; Wang, L.; Zou, J.-J. Tungsten oxides for photocatalysis, electrochemistry, and phototherapy. *Adv. Mater.* **2015**, *27*, 5309–5327. [[CrossRef](#)]
11. Kalanur, S.S.; Yoo, I.-H.; Cho, I.-S.; Seo, H. Effect of oxygen vacancies on the band edge properties of WO<sub>3</sub> producing enhanced photocurrents. *Electrochimica Acta* **2019**, *296*, 517–527. [[CrossRef](#)]
12. Upadhyay, S.B.; Mishra, R.K.; Sahay, P.P. Structural and alcohol response characteristics of Sn-doped WO<sub>3</sub> nanosheets. *Sens. Actuators B Chem.* **2014**, *193*, 19–27. [[CrossRef](#)]
13. Kalanur, S.S.; Yoo, I.-H.; Eom, K.; Seo, H. Enhancement of photoelectrochemical water splitting response of WO<sub>3</sub> by Means of Bi doping. *J. Catal.* **2018**, *357*, 127–137. [[CrossRef](#)]
14. Wang, F.; Di Valentin, C.; Pacchioni, G. Electronic and structural properties of WO<sub>3</sub>: A systematic hybrid DFT study. *J. Phys. Chem. C* **2011**, *115*, 8345–8353. [[CrossRef](#)]
15. Wang, F.; Di Valentin, C.; Pacchioni, G. Doping of WO<sub>3</sub> for photocatalytic water splitting: hints from density functional theory. *J. Phys. Chem. C* **2012**, *116*, 8901–8909. [[CrossRef](#)]
16. Kalanur, S.S.; Yoo, I.-H.; Seo, H. Fundamental investigation of Ti doped WO<sub>3</sub> photoanode and their influence on photoelectrochemical water splitting activity. *Electrochimica Acta* **2017**, *254*, 348–357. [[CrossRef](#)]
17. Kalanur, S.S.; Seo, H. Influence of molybdenum doping on the structural, optical and electronic properties of WO<sub>3</sub> for improved solar water splitting. *J. Colloid Interface Sci.* **2018**, *509*, 440–447. [[CrossRef](#)]
18. Hameed, A.; Gondal, M.A.; Yamani, Z.H. Effect of transition metal doping on photocatalytic activity of WO<sub>3</sub> for water splitting under laser illumination: role of 3d-orbitals. *Catal. Commun.* **2004**, *5*, 715–719. [[CrossRef](#)]
19. Cheng, X.F.; Leng, W.H.; Liu, D.P.; Zhang, J.Q.; Cao, C.N. Enhanced photoelectrocatalytic performance of Zn-doped WO<sub>3</sub> photocatalysts for nitrite ions degradation under visible light. *Chemosphere* **2007**, *68*, 1976–1984. [[CrossRef](#)]
20. Kalanur, S.S.; Yoo, I.-H.; Cho, I.S.; Seo, H. Niobium incorporated WO<sub>3</sub> nanotriangles: Band edge insights and improved photoelectrochemical water splitting activity. *Ceram. Int.* **2019**. [[CrossRef](#)]
21. Li, W.; Zhan, F.; Li, J.; Liu, C.; Yang, Y.; Li, Y.; Chen, Q. Enhancing photoelectrochemical water splitting by aluminum-doped plate-like WO<sub>3</sub> electrodes. *Electrochimica Acta* **2015**, *160*, 57–63. [[CrossRef](#)]
22. Kalanur, S.S.; Seo, H. Aligned nanotriangles of tantalum doped tungsten oxide for improved photoelectrochemical water splitting. *J. Alloys Compd.* **2019**, *785*, 1097–1105. [[CrossRef](#)]

23. Zhang, T.; Zhu, Z.; Chen, H.; Bai, Y.; Xiao, S.; Zheng, X.; Xue, Q.; Yang, S. Iron-doping-enhanced photoelectrochemical water splitting performance of nanostructured WO<sub>3</sub>: a combined experimental and theoretical study. *Nanoscale* **2015**, *7*, 2933–2940. [[CrossRef](#)] [[PubMed](#)]
24. Han, S.; Li, J.; Chen, X.; Huang, Y.; Liu, C.; Yang, Y.; Li, W. Enhancing photoelectrochemical activity of nanocrystalline WO<sub>3</sub> electrodes by surface tuning with Fe(III). *Int. J. Hydrog. Energy* **2012**, *37*, 16810–16816. [[CrossRef](#)]
25. Song, H.; Li, Y.; Lou, Z.; Xiao, M.; Hu, L.; Ye, Z.; Zhu, L. Synthesis of Fe-doped WO<sub>3</sub> nanostructures with high visible-light-driven photocatalytic activities. *Appl. Catal. B Environ.* **2015**, *166–167*, 112–120. [[CrossRef](#)]
26. Yang, B.; Luca, V. Enhanced long-wavelength transient photoresponsiveness of WO<sub>3</sub> induced by tellurium doping. *Chem. Commun.* **2008**, 4454–4456. [[CrossRef](#)]
27. Kalanur, S.S.; Seo, H. Intercalation of barium into monoclinic tungsten oxide nanoplates for enhanced photoelectrochemical water splitting. *Chem. Eng. J.* **2019**, *355*, 784–796. [[CrossRef](#)]
28. Cai, J.; Li, S.; Li, Z.; Wang, J.; Ren, Y.; Qin, G. Electrodeposition of Sn-doped hollow  $\alpha$ -Fe<sub>2</sub>O<sub>3</sub> nanostructures for photoelectrochemical water splitting. *J. Alloys Compd.* **2013**, *574*, 421–426. [[CrossRef](#)]
29. Zhou, Z.; Wu, S.; Qin, L.; Li, L.; Li, L.; Li, X. Modulating oxygen vacancies in Sn-doped hematite film grown on silicon microwires for photoelectrochemical water oxidation. *J. Mater. Chem. A* **2018**, *6*, 15593–15602. [[CrossRef](#)]
30. Songcan, W.; Hongjun, C.; Guoping, G.; Teera, B.; Miaoqiang, L.; Supphasin, T.; Jung-Ho, Y.; Aijun, D.; Gang, L.; Lianzhou, W. Synergistic crystal facet engineering and structural control of WO<sub>3</sub> films exhibiting unprecedented photoelectrochemical performance. *Nano Energy* **2016**, *24*, 94–102.
31. Kalanur, S.S.; Hwang, Y.J.; Chae, S.Y.; Joo, O.S. Facile growth of aligned WO<sub>3</sub> nanorods on FTO substrate for enhanced photoanodic water oxidation activity. *J. Mater. Chem. A* **2013**, *1*, 3479–3488. [[CrossRef](#)]
32. Qi, J.; Chen, K.; Xing, Y.; Fan, H.; Zhao, H.; Yang, J.; Li, L.; Yan, B.; Zhou, J.; Guo, L.; et al. Application of 3D hierarchical monoclinic-type structural Sb-doped WO<sub>3</sub> towards NO<sub>2</sub> gas detection at low temperature. *Nanoscale* **2018**, *10*, 7440–7450. [[CrossRef](#)] [[PubMed](#)]
33. Xia, W.; Wang, H.; Zeng, X.; Han, J.; Zhu, J.; Zhou, M.; Wu, S. High-efficiency photocatalytic activity of type II SnO/Sn<sub>3</sub>O<sub>4</sub> heterostructures via interfacial charge transfer. *Cryst. Eng. Comm.* **2014**, *16*, 6841–6847. [[CrossRef](#)]
34. Matsumoto, Y.; Omae, M.; Watanabe, I.; Sato, E. Photoelectrochemical properties of the Zn-Ti-Fe spinel oxides. *J. Electrochem. Soc.* **1986**, *133*, 711–716. [[CrossRef](#)]
35. Guo, W.; Chemelewski, W.D.; Mabayoje, O.; Xiao, P.; Zhang, Y.; Mullins, C.B. Synthesis and characterization of CuV<sub>2</sub>O<sub>6</sub> and Cu<sub>2</sub>V<sub>2</sub>O<sub>7</sub>: Two photoanode candidates for photoelectrochemical water oxidation. *J. Phys. Chem. C* **2015**, *119*, 27220–27227. [[CrossRef](#)]

